Supplementary Information: Simulating unsteady flows on a superconducting quantum processor

Zhaoyuan Meng,[1,*] Jiarun Zhong,[2,*] Shibo Xu,[2,*] Ke Wang,[2] Jiachen Chen,[2] Feitong Jin,[2] Xuhao Zhu,[2] Yu Gao,[2] Yaozu Wu,[2] Chuanyu Zhang,[2] Ning Wang,[2] Yiren Zou,[2] Aosai Zhang,[2] Zhengyi Cui,[2] Fanhao Shen,[2] Zehang Bao,[2] Zitian Zhu,[2] Ziqi Tan,[2] Tingting Li,[2] Pengfei Zhang,[2] Shiying Xiong,[3] Hekang Li,[2] Qiujiang Guo,[2] Zhen Wang,[2] Chao Song,[2,†] H. Wang,[2] and Yue Yang[1,4,‡]

[1]*State Key Laboratory for Turbulence and Complex Systems, College of Engineering, Peking University, Beijing 100871, China*

[2]*School of Physics, ZJU-Hangzhou Global Scientific and Technological Innovation Center, and Zhejiang Key Laboratory of Micro-nano Quantum Chips and Quantum Control, Zhejiang University, Hangzhou 310027, China*

[3]*Department of Engineering Mechanics, School of Aeronautics and Astronautics, Zhejiang University, Hangzhou 310027, China*

[4]*HEDPS-CAPT, Peking University, Beijing 100871, China*

CONTENTS

1. SUPPLEMENTARY NOTE 1: QUANTUM REPRESENTATION OF FLUID FLOWS

A. Madelung transform for potential flows

In quantum mechanics, the probability current for a one-component wave function $\psi(\boldsymbol{x}, t)$ is given by

$$\boldsymbol{J}(\boldsymbol{x}, t) \equiv \frac{1}{2m}(\psi^* \hat{\boldsymbol{p}}\psi - \psi\hat{\boldsymbol{p}}\psi^*), \tag{S1}$$

where $\hat{\boldsymbol{p}}$ is the momentum operator, m is the particle mass, and "$*$" denotes the complex conjugate. In the coordinate representation, we have $\hat{\boldsymbol{p}} = -i\hbar\boldsymbol{\nabla}$ with the imaginary unit i and Planck constant $\hbar$. A particle subject to a real potential V obeys the

* These authors contributed equally

† chaosong@zju.edu.cn

‡ yyg@pku.edu.cn

time-dependent Schrödinger equation

$$i\hbar\frac{\partial}{\partial t}\psi(\boldsymbol{x},t) = \Big(-\frac{\hbar^2}{2m}\nabla^2 + V\Big)\psi(\boldsymbol{x},t). \tag{S2}$$

Combining Eqs. (S1) and (S2) yields the conservation law for the probability density $\rho \equiv |\psi|^2$ as

$$\frac{\partial\rho}{\partial t} + \boldsymbol{\nabla}\cdot(\rho\boldsymbol{u}) = 0, \tag{S3}$$

which is identical to the continuity equation in fluid mechanics, with a "velocity" $\boldsymbol{u} \equiv \boldsymbol{J}/\rho$.

The Madelung transform [S1] establishes a correspondence between quantum mechanics and fluid mechanics. The probability density and the probability current in quantum mechanics are analogous to the mass density and momentum in fluid mechanics, respectively. The Planck constant in this hydrodynamic representation is a scaling parameter instead of a physical constant.

Applying the Madelung transform to Eq. (S2) yields the momentum equation

$$\frac{\partial\boldsymbol{u}}{\partial t} + \boldsymbol{u}\cdot\boldsymbol{\nabla}\boldsymbol{u} = -\frac{1}{m}\boldsymbol{\nabla}V + \frac{\hbar^2}{2m^2}\boldsymbol{\nabla}\frac{\nabla^2\sqrt{\rho}}{\sqrt{\rho}} \tag{S4}$$

for a fluid flow. The density and velocity are given by

$$\rho = |\psi|^2, \quad \boldsymbol{u} = \frac{i\hbar}{2m}\frac{\psi\boldsymbol{\nabla}\psi^* - \psi^*\boldsymbol{\nabla}\psi}{\rho}. \tag{S5}$$

The second term on the right-hand side of Eq. (S4) is known as the Bohm potential. Substituting $\psi = \sqrt{\rho}e^{i\phi/\hbar}$ into Eq. (S5), the velocity becomes $\boldsymbol{u} = \boldsymbol{\nabla}\phi/m$, so Eq. (S4) is the compressible Euler equation for a potential flow with zero vorticity.

B. Generalized Madelung transform for vortical flows

To introduce finite vorticity to a fluid flow, we consider a two-component wave function

$$|\psi_\pm\rangle = \begin{bmatrix}\psi_+\\ \psi_-\end{bmatrix}, \tag{S6}$$

where ψ_+ and ψ_- denote the complex spin-up and -down components, respectively [S2–S4]. The probabilistic current in Eq. (S1) is generalized to

$$\boldsymbol{J} \equiv \frac{\hbar}{m}\langle\boldsymbol{\nabla}\psi_\pm, i\psi_\pm\rangle_{\mathbb{R}}, \tag{S7}$$

where $\langle\cdot,\cdot\rangle_{\mathbb{R}}$ is the real inner product defined as $\langle\phi,\psi\rangle_{\mathbb{R}} \equiv \sum_{i=1}^2(x_i\alpha_i + y_i\beta_i)$ for $\phi = [x_1+iy_1, x_2+iy_2]^{\mathrm{T}}$ and $\psi = [\alpha_1+i\beta_1, \alpha_2+i\beta_2]^{\mathrm{T}}$. Using the generalized Madelung transform [S4], we define the flow velocity

$$\boldsymbol{u} \equiv \frac{\boldsymbol{J}}{\rho} = \frac{\hbar}{m}\frac{\langle\boldsymbol{\nabla}\psi_\pm, i\psi_\pm\rangle_{\mathbb{R}}}{\langle\psi_\pm,\psi_\pm\rangle_{\mathbb{R}}}, \tag{S8}$$

where

$$\rho \equiv \langle\psi_\pm,\psi_\pm\rangle_{\mathbb{R}} = |\psi_+|^2 + |\psi_-|^2 \tag{S9}$$

is the mass density. The flow field given by Eq. (S8) has finite vorticity, i.e., $\boldsymbol{\omega} \equiv \boldsymbol{\nabla}\times\boldsymbol{u} \neq \boldsymbol{0}$.

Then, we consider a two-component time-dependent Schrödinger equation

$$i\hbar\frac{\partial}{\partial t}|\psi_\pm\rangle = \Big(-\frac{\hbar^2}{2m}\nabla^2 + V\Big)|\psi_\pm\rangle \tag{S10}$$

with a real-valued potential V. The continuity equation follows from the conservation of probability current. The momentum equation is obtained as [S4]

$$\frac{\partial\boldsymbol{u}}{\partial t} + \boldsymbol{u}\cdot\boldsymbol{\nabla}\boldsymbol{u} = -\boldsymbol{\nabla}\Big(\frac{V}{m} - \frac{\hbar^2|\boldsymbol{\nabla}\boldsymbol{s}|^2}{8m^2\rho^2}\Big) - \frac{\hbar}{m\rho}\boldsymbol{\nabla}(\boldsymbol{\zeta}\cdot\boldsymbol{s}) + \frac{\hbar}{m\rho}\boldsymbol{\nabla}\boldsymbol{s}\cdot\boldsymbol{\zeta}, \tag{S11}$$

where we define the spin vector

$$\boldsymbol{s} = (|\psi_+|^2 - |\psi_-|^2, i(\psi_+^*\psi_- - \psi_+\psi_-^*), \psi_+^*\psi_- + \psi_+\psi_-^*), \tag{S12}$$

and a vector

$$\boldsymbol{\zeta} = -\frac{1}{4}\boldsymbol{\nabla}\cdot\left(\frac{\boldsymbol{\nabla s}}{\rho}\right). \tag{S13}$$

Equation (S11) can be re-expressed as a standard compressible Euler equation

$$\frac{\partial \boldsymbol{u}}{\partial t} + \boldsymbol{u}\cdot\boldsymbol{\nabla u} = -\frac{1}{\rho}\boldsymbol{\nabla} p - \boldsymbol{\nabla} U_F + \boldsymbol{f}, \tag{S14}$$

with the "quantum pressure" $p = \hbar\boldsymbol{\zeta}\cdot\boldsymbol{s}/m$, an effective potential $U_F = V/m - \hbar^2|\boldsymbol{\nabla s}|^2/(8m^2\rho^2)$, and a body force $\boldsymbol{f} = \hbar\boldsymbol{\nabla s}\cdot\boldsymbol{\zeta}/(m\rho)$.

2. SUPPLEMENTARY NOTE 2: CONSTRUCTION OF QUANTUM CIRCUITS

A. Initial state preparation

We use two typical simple flows to demonstrate the capability of quantum simulation of fluid dynamics on the NISQ device. Their initial condition and evolution are described below.

The first case is a 2D diverging compressible potential flow within a periodic domain $\boldsymbol{x} \in [-\pi,\pi]^2$. The initial wave function is

$$\psi(\boldsymbol{x}, 0) = e^{-y^2/(2\varrho^2)+ix}, \tag{S15}$$

with a geometric parameter $\varrho = 1$. For clarity, we omit the normalization constant in Eq. (S15) for the unity encoded quantum state. Applying the Madelung transform to Eq. (S15) yields the initial density and velocity

$$\rho(\boldsymbol{x}, 0) = e^{-y^2/\varrho^2} \quad \text{and} \quad \boldsymbol{u}(\boldsymbol{x}, 0) = \boldsymbol{e}_x, \tag{S16}$$

where $\{\boldsymbol{e}_x, \boldsymbol{e}_y\}$ are the Cartesian unit vectors. The initial condition in Eq. (S15) describes a flow which is uniform in the x-direction and has a Gaussian profile of the density in the y-direction. The thickness of the high-density layer around $y = 0$ is determined by ϱ.

Applying the Fourier transform, the time integration for the initial value problem in spectral space, and then the inverse Fourier transform, we obtain the exact solution to Eq. (S2) as

$$\begin{aligned}\psi(\boldsymbol{x}, t) &= \frac{1}{(2\pi)^2}\sum_{\boldsymbol{k}}\left(\int_{[-\pi,\pi]^2} e^{-y^2/(2\varrho^2)+ix} e^{-i\boldsymbol{k}\cdot\boldsymbol{x}}\,\mathrm{d}\boldsymbol{x}\right)e^{-ik^2t/2+i\boldsymbol{k}\cdot\boldsymbol{x}}\\ &= \frac{\varrho}{\sqrt{8\pi}}\sum_{k_2=-\infty}^{\infty}\left[\mathrm{erf}\left(\frac{\pi - i\varrho k_2}{\sqrt{2}\varrho}\right) + \mathrm{erf}\left(\frac{\pi + i\varrho k_2}{\sqrt{2}\varrho}\right)\right]e^{-\varrho^2k_2^2/2 - i(k_2^2+1)t/2 + i(x+k_2y)},\end{aligned} \tag{S17}$$

where $\boldsymbol{k} = (k_1, k_2)$, $k_i = 0, \pm1, \pm2, \cdots$, $i = 1, 2$ denotes the wavenumber vector, $k = |\boldsymbol{k}|$ the wavenumber magnitude, and $\mathrm{erf}(z) \equiv \frac{2}{\sqrt{\pi}}\int_0^z e^{-t^2}\,\mathrm{d}t$ the error function.

The second case is a vortical flow with an artificial body force governed by Eq. (S14). We apply the rational maps [S5] to construct a 2D vortex at the center of the periodic domain $\boldsymbol{x} \in [-\pi,\pi]^2$. First, we define the vortex decay rate by

$$f(r) = e^{-(r/r_0)^4}, \tag{S18}$$

with the radial distance $r = \sqrt{x^2 + y^2}$ and the vortex size $r_0 = 3$. Then, we define a pair of complex-valued functions

$$u = \frac{2(x+iy)f(r)}{1+r^2}, \quad v = \frac{i[r^2 + 1 - 2f(r)]}{1+r^2}. \tag{S19}$$

Finally, we specify the initial spin-up and -down components

$$\psi_+(\boldsymbol{x}, 0) = \frac{u}{\sqrt{|u|^2 + |v|^4}}, \quad \psi_-(\boldsymbol{x}, 0) = \frac{v^2}{\sqrt{|u|^2 + |v|^4}}. \tag{S20}$$

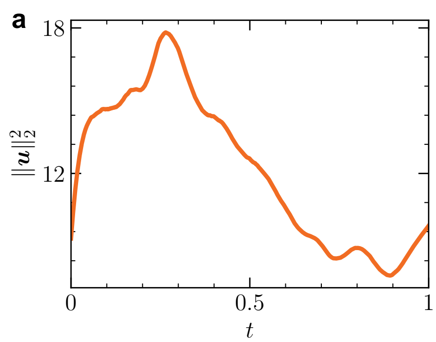

Figure S1. Evolution of (a) the total kinetic energy and (b) enstrophy for the 2D vortex in Eqs. (S21) and (S22).

Note that we omit the normalization constant in Eq. (S20).

The exact solutions to Eq. (S10) are

$$\psi_+(\boldsymbol{x},t) = \frac{1}{(2\pi)^2}\sum_{\boldsymbol{k}}\left(\int_{[-\pi,\pi]^2}\frac{u}{\sqrt{|u|^2+|v|^4}}e^{-i\boldsymbol{k}\cdot\boldsymbol{x}}\,\mathrm{d}\boldsymbol{x}\right)e^{-ik^2t/2+i\boldsymbol{k}\cdot\boldsymbol{x}}, \tag{S21}$$

and

$$\psi_-(\boldsymbol{x},t) = -\frac{1}{(2\pi)^2}\sum_{\boldsymbol{k}}\left(\int_{[-\pi,\pi]^2}\frac{v^2}{\sqrt{|u|^2+|v|^4}}e^{-i\boldsymbol{k}\cdot\boldsymbol{x}}\,\mathrm{d}\boldsymbol{x}\right)e^{-ik^2t/2+i\boldsymbol{k}\cdot\boldsymbol{x}}. \tag{S22}$$

With Eqs. (S21) and (S22), we obtain the velocity field from Eq. (S8). Subsequently, we calculate the vorticity by computing the curl of this velocity field.

Figure S1 shows the evolution of the total kinetic energy and enstrophy for the 2D vortex in Eqs. (S21) and (S22). Due to the artificial body force, they both initially increase and subsequently decreases.

B. Evolution of quantum state

For potential flows, the wave function is encoded by the state vector

$$|\psi(t)\rangle = \frac{1}{\|\psi\|_2}\sum_{k=0}^{N_y-1}\sum_{j=0}^{N_x-1}\psi(x_j,y_k,t)|j,k\rangle, \tag{S23}$$

where $N_x = 2^{n_x}$ and $N_y = 2^{n_y}$ denote numbers of grid points along the x- and y-directions, corresponding to numbers n_x and n_y of qubits, respectively, and

$$\|\psi\|_2 = \sqrt{\sum_{j=0}^{N_x-1}\sum_{k=0}^{N_y-1}|\psi(x_j,y_k,t)|^2} \tag{S24}$$

represents the normalization coefficient. To avoid deep circuits due to iterations in time marching, we impose $V = 0$ in Eq. (S2), signifying the absence of conservative body forces in the fluid flow. This condition allows the time step to be arbitrarily large, enabling a “one-shot” solution [S6] for a given time t without temporal discretization and intermediate measurement.

Thus, the state vector at t is determined by

$$|\psi(t)\rangle = \left(\widehat{\mathrm{QFT}}_x^\dagger e^{-i\hat{k}_x^2t/2}\widehat{\mathrm{QFT}}_x\right)\otimes\left(\widehat{\mathrm{QFT}}_y^\dagger e^{-i\hat{k}_y^2t/2}\widehat{\mathrm{QFT}}_y\right)|\psi(0)\rangle, \tag{S25}$$

with the quantum Fourier transform (QFT) [S7, S8]

$$\widehat{\mathrm{QFT}}:\ |j\rangle \to \frac{1}{\sqrt{2^n}}\sum_{k=0}^{2^n-1}e^{2\pi i\frac{jk}{2^n}}|k\rangle, \tag{S26}$$

the wavenumber vector $\hat{\boldsymbol{k}} = (\hat{k}_x, \hat{k}_y)$, and

$$\hat{k}_\alpha = \mathrm{diag}(0, 1, 2, \cdots, 2^{n_\alpha - 1} - 2, 2^{n_\alpha - 1} - 1, -2^{n_\alpha - 1}, -2^{n_\alpha - 1} + 1, \cdots, -1),\ \alpha = x, y. \tag{S27}$$

We rewrite Eq. (S27) as

$$\hat{k}_\alpha = \mathrm{diag}(0, 1, \cdots, 2^{n_\alpha} - 1) - 2^{n_\alpha} \begin{bmatrix} 0 & 0 \\ 0 & 1 \end{bmatrix} \otimes I_{2^{n_\alpha - 1}} = \mathrm{diag}(0, 1, \cdots, 2^{n_\alpha} - 1) - 2^{n_\alpha - 1} \left(I_{2^{n_\alpha}} - \hat{Z} \otimes I_{2^{n_\alpha - 1}} \right), \tag{S28}$$

where $\hat{Z} = \mathrm{diag}(1, -1)$ denotes the Pauli-Z gate, and $I_{2^{n_\alpha}}$ the $2^{n_\alpha} \times 2^{n_\alpha}$ identity matrix.

Then, we prove the *proposition*

$$P(n_\alpha):\ \mathrm{diag}(0, 1, \cdots, 2^{n_\alpha} - 1) = \frac{1}{2}\Big[(2^{n_\alpha} - 1) I_{2^{n_\alpha}} - \sum_{j=1}^{n_\alpha} 2^{n_\alpha - j} I_{2^{j-1}} \otimes \hat{Z} \otimes I_{2^{n_\alpha - j}}\Big] \tag{S29}$$

by mathematical induction.

Proof 1 *Base case: for $n_\alpha = 1$, the identity*

$$\mathrm{diag}(0, 1) = \frac{1}{2}(I_2 - \hat{Z}) \tag{S30}$$

verifies $P(1)$.

Induction step: we will show $P(k+1)$ from $P(k)$ for any positive integer k. Assume for a given value $k \geqslant 1$, the single case $P(k)$ is true, i.e.,

$$\mathrm{diag}(0, 1, \cdots, 2^k - 1) = \frac{1}{2}\Big[(2^k - 1) I_{2^k} - \sum_{j=1}^{k} 2^{k-j} I_{2^{j-1}} \otimes \hat{Z} \otimes I_{2^{k-j}}\Big]. \tag{S31}$$

For $k + 1$, we deduce

$$\begin{aligned} \mathrm{diag}(0, 1, \cdots, 2^{k+1} - 1) &= \begin{bmatrix} \mathrm{diag}(0, 1, \cdots, 2^k - 1) & \mathbf{0} \\ \mathbf{0} & \mathrm{diag}(0, 1, \cdots, 2^k - 1) + 2^k I_{2^k} \end{bmatrix} \\ &= I_2 \otimes \mathrm{diag}(0, 1, \cdots, 2^k - 1) + 2^k \begin{bmatrix} 0 & 0 \\ 0 & 1 \end{bmatrix} \otimes I_{2^k} \\ &= \frac{1}{2}\Big[(2^k - 1) I_{2^{k+1}} - \sum_{j=2}^{k+1} 2^{k+1-j} I_{2^{j-1}} \otimes \hat{Z} \otimes I_{2^{k+1-j}}\Big] + 2^k \frac{I_2 - \hat{Z}}{2} \otimes I_{2^k} \\ &= \frac{1}{2}\Big[(2^{k+1} - 1) I_{2^{k+1}} - \sum_{j=1}^{k+1} 2^{k+1-j} I_{2^{j-1}} \otimes \hat{Z} \otimes I_{2^{k+1-j}}\Big]. \end{aligned} \tag{S32}$$

So $P(k+1)$ is true, and the proposition $P(n_\alpha)$ in Eq. (S29) *is true for all positive integers n_α.*

Substituting Eq. (S29) into Eq. (S28), we obtain

$$\hat{k}_\alpha = -\frac{1}{2}\Big(I_{2^{n_\alpha}} + \sum_{j=1}^{n_\alpha} 2^{n_\alpha - j} \hat{Z}_j\Big) + 2^{n_\alpha} \hat{Z}_1,\ \alpha = x, y, \tag{S33}$$

with the phase-shift gate $\hat{Z}_j = I_{2^{j-1}} \otimes \hat{Z} \otimes I_{2^{n_\alpha - j}}$ at the j-th qubit.

Then, from Eq. (S33), the momentum operator

$$e^{-i\hat{k}_\alpha^2 t/2} = \exp\Big\{ -\frac{it}{2}\Big[-\frac{1}{2}\Big(I_{2^{n_\alpha}} + \sum_{j=1}^{n_\alpha} 2^{n_\alpha - j} \hat{Z}_j\Big) + 2^{n_\alpha} \hat{Z}_1 \Big]^2 \Big\} \tag{S34}$$

is decomposed into the single-qubit gate

$$R_z(\theta) \equiv e^{-i\theta \hat{Z}/2} = \begin{bmatrix} e^{-i\theta/2} & 0 \\ 0 & e^{i\theta/2} \end{bmatrix} \tag{S35}$$

Table S1. Fidelity of results generated by CPFlow.

Target	State encoding			Evolution	
	Diverging flow	2D vortex (ψ_+)	2D vortex (ψ_-)	$t = \pi/4$	$t = \pi/2$
1 − F	8×10^{-6}	8×10^{-3}	8×10^{-3}	5×10^{-7}	8×10^{-10}

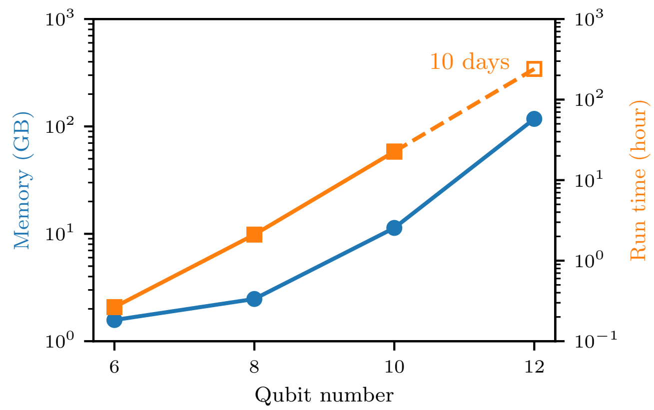

Figure S2. Computational resources (on a classical computer) required for obtaining state encoding circuits with CPFlow. The estimated run time for 12 qubits is based on extrapolation, as illustrated by the dashed line.

and the two-qubit gate

$$\mathrm{ZZ}(\theta) \equiv e^{-i\theta \hat{Z}\otimes\hat{Z}/2} = \mathrm{diag}(e^{-i\theta/2}, e^{i\theta/2}, e^{i\theta/2}, e^{-i\theta/2}) = \mathrm{CNOT}[I_2 \otimes R_z(\theta)]\mathrm{CNOT}, \tag{S36}$$

where CNOT denotes the controlled-NOT gate. Note that the global phase from $I_{2^{n_\alpha}}$ can be ignored.

For vortical flows, an additional qubit can be added to encode the spin state [S4] into the $n_x + n_y + 1$ qubits. Instead, we split the two components in $\psi_\pm$, and treat ψ_+ or ψ_- as ψ for potential flows, due to the uncoupled nature of the two components in Eq. (S10). This permits utilization of the identical qubit array as in potential flow and a shorter circuit for improving experimental outcomes.

C. Circuit optimization

The original circuits for initial state preparation and evolution may contain CZ gates between arbitrary two qubits. Constrained by the layout topology of our device, only CZ gates between adjacent qubits are allowed, necessitating further circuit transpilations.

In this work, considering the limited fidelities of the quantum gates on our device, we use CPFlow [S9] to obtain approximate circuits that fit the native gate set and device topology, meanwhile minimize the number of CZ gates. This program takes connections between qubits, the threshold, and the loss function based on the targeting state or unitary matrix as main input. Here we choose 1 − F as the loss function where F is the fidelity between the target and result. Based on the input connections, it randomly generate entangling blocks containing the gate set $\{\mathrm{CP}, R_x, R_y, R_z\}$, where CP denotes controlled-phase gate and R_i represents rotation gates around the axis i, and adjust angles of each gate to minimize the loss function. The optimization procedure ends when the threshold is reached. The fidelity of results generated by CPFlow is listed in Tab. S1. The classical computational resources required for obtaining state encoding circuits is shown in Fig. S2, which can be prohibitive for large $n > 10$.

3. SUPPLEMENTARY NOTE 3: EXPERIMENTAL DETAILS

A. Device information

Our experiments are performed on a quantum processor with frequency-tunable transmon qubits encapsulated in a 11×11 square lattice and tunable couplers between adjacent qubits, with the overall design similar to that in Ref. [S10] (see Fig. S3).

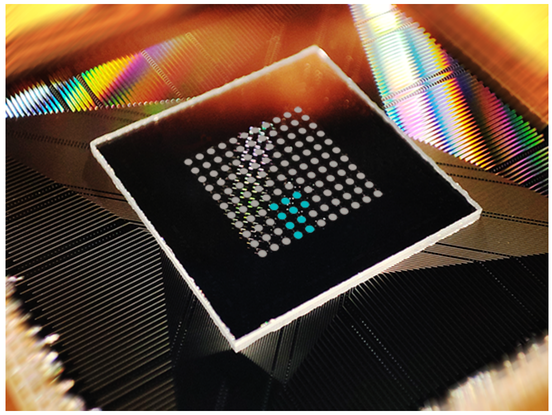

Figure S3. A photograph of the present flip-chip superconducting quantum processor, which contains a square lattice of 11×11 qubits (circles). The 10 qubits used in our experiment are highlighted in cyan.

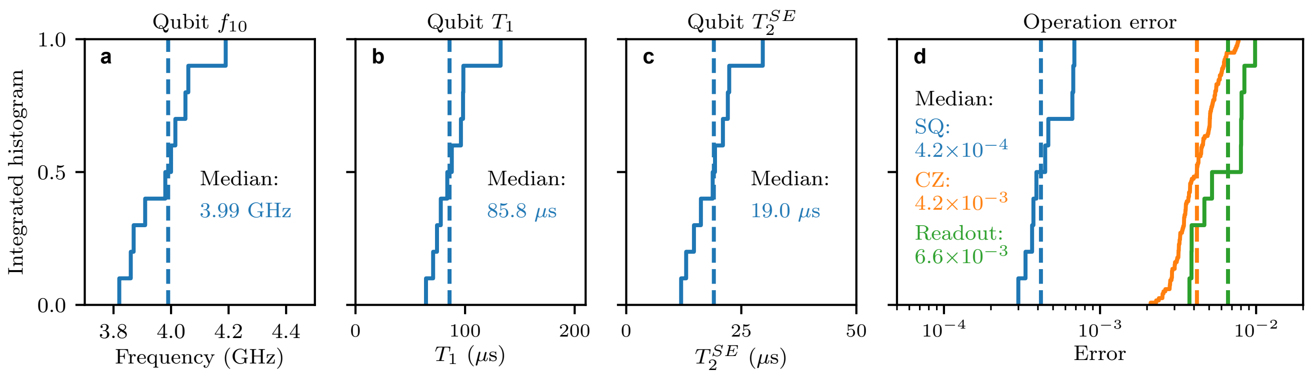

Figure S4. Integrated histograms of various device performance parameters. (a) Qubit idle frequency. (b) Qubit relaxation time measured at the idle frequency. (c) Qubit dephasing time measured using spin echo sequence. (d) Simultaneous operation errors of single-qubit gates (blue), two-qubit CZ gates (orange), and readout (green). Dashed lines indicate the median values. The errors of quantum gates are Pauli errors obtained through simultaneous cross-entropy benchmarking, and the readout error is calculated as $e_r = 1 - (f_0 + f_1)/2$ with $f_{0(1)}$ denoting the measure fidelities of the state $|0\rangle$ ($|1\rangle$).

The maximum resonance frequencies of the qubit and coupler are around 4.5 GHz and 9.0 GHz, respectively. The effective coupling between two neighboring qubits can be dynamically activated by biasing the sandwiched coupler down close to qubits' interaction frequency. Each qubit capacitively couples to its own readout resonator at the frequency of around 6.5 GHz for dispersively readout. As illustrated in Fig. 1, ten qubits are used in our experiments, with the characterized properties summarized in Fig. S4.

B. Circuit implementation

We employ the native gate set $\{U(\theta,\varphi,\lambda), \mathrm{CZ}\}$ to implement the desired experimental circuits, where $U(\theta,\varphi,\lambda) = R_z(\varphi)R_y(\theta)R_z(\lambda)$ denotes a generic single-qubit gate with three Euler angles, and CZ denotes the two-qubit CZ gate that fits the layout topology of our device. In practice, each generic single-qubit gate is achieved with a virtual Z rotation [S11] followed by a 30-ns long microwave pulse shaped with DRAG technique [S12], which can be formulated as $R_{\varphi+\pi/2}(\theta)R_z(\varphi+\lambda)$ where the subscript $\varphi+\pi/2$ refers to the angle of the equatorial rotation axis with respect to the x-axis. We realize two-qubit CZ gates by bringing $|11\rangle$ and $|02\rangle$ (or $|20\rangle$) of the qubit pairs in near resonance and activating the coupling for a specific time of 30 ns to achieve a complete cycle between $|11\rangle$ and $|02\rangle$ (or $|20\rangle$), with the calibration procedure detailed in Ref. [S13].

Each experimental circuit is aligned as a staggered arrangement of single- and two-qubit gate layers, with a typical experimental circuit shown in Fig. S5 and all aligned circuit depths listed in Tab. S2. CZ gate parameters are optimized for each two-qubit gate layer. We perform simultaneous cross entropy benchmarking (XEB) [S14, S15] to characterize the performance of the quantum gates used in circuits with the statistical result shown in Fig. S4(d).

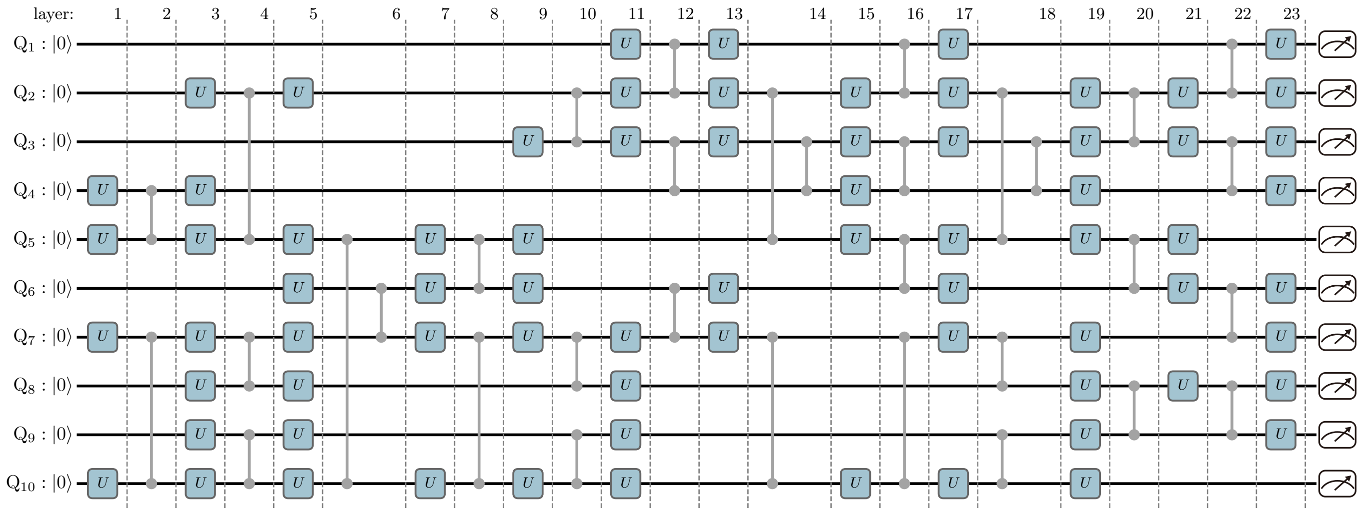

Figure S5. Experimental circuit for encoding the spin-up component for the 2D vortex. Starting with the ground state $|0\rangle^{\otimes 10}$, we apply parallel single- and two-qubit gates layer by layer with the circuit depth up to 23. In practice, each layer of parallel single-qubit (two-qubit) gate requires a duration of 30 (40) ns. Hence, the total execution time is 810 ns, which is still much shorter than the median lifetime of qubits around 90 μs. At the end of the circuit, we measure all qubits simultaneously to reconstruct the density and momentum fields. Each round rectangle with label U denotes a generic single-qubit gate.

Table S2. Depths of aligned circuits.

	$t = 0$	$t = \pi/4$	$t = \pi/2$
Diverging flow	13	33	19
2D vortex (ψ_+)	23	45	29
2D vortex (ψ_-)	27	49	29

C. Measurement of quantum state

Here we derive the matrix elements of the measurement operator of density and momentum. To facilitate this analysis, we introduce $\phi(m,l) = \psi_{2^{n_x}m+l}$, where the indices $l = 0, 1, \ldots, 2^{n_x} - 1$ and $m = 0, 1, \ldots, 2^{n_y} - 1$ denote the discrete coordinates in the x and y directions, respectively. Consequently, the density is measured as

$$\rho(m,l) = \phi^*(m,l)\phi(m,l) = \psi^*_{2^{n_x}m+l}\psi_{2^{n_x}m+l} = \langle\psi|\,\hat{\rho}^{(m,l)}\,|\psi\rangle, \tag{S37}$$

and the matrix elements of the measurement operator are

$$\hat{\rho}^{(m,l)}_{j,k} = \delta_{j,\,2^{n_x}m+l}\delta_{2^{n_x}m+l,\,k}. \tag{S38}$$

Note that the whole density field can be obtained from a single measurement.

Extracting momentum field is much more complicated. We employ the finite difference method to approximate derivatives in the momentum expression in Eq. (S5). In practice, we replace non-bounded (bounded) derivatives with central (forward or backward) differences. The derivation for non-bounded momentum is provided below.

The momentum is re-expressed as

$$\begin{aligned}
\boldsymbol{J}(m,l) &= \frac{i}{2}\left[\phi(m,l)\boldsymbol{\nabla}\phi^*(m,l) - \phi^*(m,l)\boldsymbol{\nabla}\phi(m,l)\right] \\
&\approx \frac{i}{4\Delta x}\left[\left(\phi^*(m,l+1) - \phi^*(m,l-1)\right)\phi(m,l) - \phi^*(m,l)\left(\phi(m,l+1) - \phi(m,l-1)\right)\right]\boldsymbol{e}_x \\
&\quad + \frac{i}{4\Delta y}\left[\left(\phi^*(m+1,l) - \phi^*(m-1,l)\right)\phi(m,l) - \phi^*(m,l)\left(\phi(m+1,l) - \phi(m-1,l)\right)\right]\boldsymbol{e}_y \\
&= \frac{i}{4\Delta x}\left[\phi^*(m,l+1)\phi(m,l) - \phi^*(m,l-1)\phi(m,l) - \phi^*(m,l)\phi(m,l+1) + \phi^*(m,l)\phi(m,l-1)\right]\boldsymbol{e}_x \\
&\quad + \frac{i}{4\Delta y}\left[\phi^*(m+1,l)\phi(m,l) - \phi^*(m-1,l)\phi(m,l) - \phi^*(m,l)\phi(m+1,l) + \phi^*(m,l)\phi(m-1,l)\right]\boldsymbol{e}_y \\
&= \frac{i}{4\Delta x}\left(\psi^*_{2^{n_x}m+l+1}\psi_{2^{n_x}m+l} - \psi^*_{2^{n_x}m+l-1}\psi_{2^{n_x}m+l} - \psi^*_{2^{n_x}m+l}\psi_{2^{n_x}m+l+1} + \psi^*_{2^{n_x}m+l}\psi_{2^{n_x}m+l-1}\right)\boldsymbol{e}_x \\
&\quad + \frac{i}{4\Delta y}\left(\psi^*_{2^{n_x}(m+1)+l}\psi_{2^{n_x}m+l} - \psi^*_{2^{n_x}(m-1)+l}\psi_{2^{n_x}m+l} - \psi^*_{2^{n_x}m+l}\psi_{2^{n_x}(m+1)+l} + \psi^*_{2^{n_x}m+l}\psi_{2^{n_x}(m-1)+l}\right)\boldsymbol{e}_y \\
&= \langle\psi|\,\hat{\boldsymbol{J}}^{(m,l)}\,|\psi\rangle,
\end{aligned} \tag{S39}$$

with matrix elements

$$\begin{aligned}
\hat{\boldsymbol{J}}^{(m,l)}_{j,k} = \frac{i}{2}\Bigg[&\delta_{2^{n_x}m+l,k}\left(\frac{\delta_{j,2^{n_x}m+l+1} - \delta_{j,2^{n_x}m+l-1}}{2\Delta x}\boldsymbol{e}_x + \frac{\delta_{j,2^{n_x}(m+1)+l} - \delta_{j,2^{n_x}(m-1)+l}}{2\Delta y}\boldsymbol{e}_y\right) \\
&- \delta_{j,2^{n_x}m+l}\left(\frac{\delta_{2^{n_x}m+l+1,k} - \delta_{2^{n_x}m+l-1,k}}{2\Delta x}\boldsymbol{e}_x + \frac{\delta_{2^{n_x}(m+1)+l,k} - \delta_{2^{n_x}(m-1)+l,k}}{2\Delta y}\boldsymbol{e}_y\right)\Bigg],
\end{aligned} \tag{S40}$$

grid spacings $\Delta x = 2\pi/2^{n_x}$ and $\Delta y = 2\pi/2^{n_y}$, the Kronecker delta δ, and Cartesian unit vectors $\{\boldsymbol{e}_x, \boldsymbol{e}_y\}$.

For vortical flows, we measure $\rho_\pm(m,l)$ and $\boldsymbol{J}_\pm(m,l)$ using the same method, and then compute $\boldsymbol{u} = (\boldsymbol{J}_+ + \boldsymbol{J}_-)/(\rho_+ + \rho_-)$ and $\omega = \partial u_y/\partial x - \partial u_x/\partial y$.

In principle, each generic n-qubit observable O can be decomposed as a sum of Pauli strings

$$O = \sum_{j=0}^{4^n-1} \frac{\mathrm{Tr}(OP_j)}{2^n} P_j, \quad P_j \in \{\sigma^{\otimes n}\} \tag{S41}$$

which requires an exponentially increasing number of measurements. However, for the momentum operator $\hat{\boldsymbol{J}}^{(m,l)}$, only a few terms in Eq. (S41) have non-zero coefficients, which significantly reduce the experimental runtime. As a result, 5120 Pauli strings are required to reconstruct the momentum field. Furthermore, since some local Pauli strings, e.g., ZIZZIXXXYX, can be calculated from the measured probability distribution of certain global Pauli strings, e.g., ZZZZZXXXYX, the measurement number is eventually reduced to 62. Here we plot the first 20 Pauli string expectation values in decreasing order for the diverging flow case in Fig. S6, which shows decent agreement with the exact solution.

In summary, we perform 63 measurements to reconstruct the density field and momentum field for each circuit. Each measurement involves 10^5 single shots to build the probability distribution, consuming approximately 20 s at a sampling rate of 5 kHz. The experiment is repeated five times for each flow case. The average results for all flow cases in main text are shown in Fig. S7.

4. SUPPLEMENTARY NOTE 4: EFFECTS OF QUANTUM ERRORS

Although the experimental results on the superconducting processor capture the major features of fluid dynamics in all flow cases, there are some notable artifacts, such as regular stripe patterns in the reconstructed flow fields in Fig. 2(c). Here we investigate the origins of these artifacts with numerical simulations.

A. Stripe-like artifacts

The ability of the finite number of qubits to encode an exponentially large fluid state suggests that local perturbations can exert a global influence on the encoded flow field. As illustrated in Fig. S8(a), we demonstrate this phenomenon by applying an extra error gate after each single-qubit gate on a certain qubit. The numerical simulation results exhibit different regular stripe patterns depending on the choice of the error qubit in Figs. S8(b) and (c).

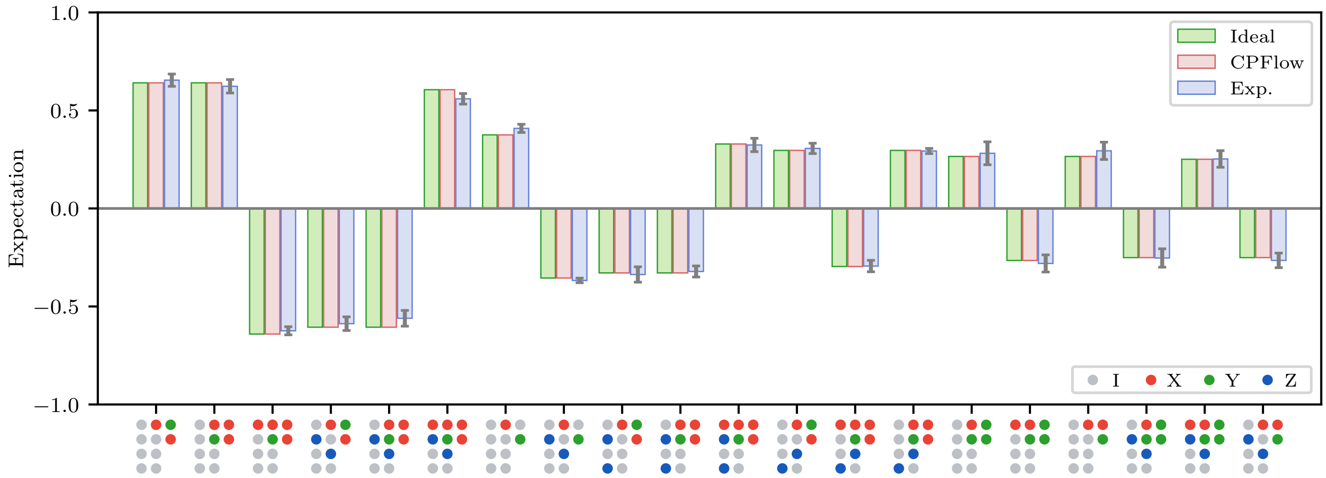

Figure S6. Expectation values of decomposed Pauli strings for the initial state of the diverging flow. We plot the first 20 expectation values obtained from the exact solution (green), CPFlow simulation (red), and experiment (blue) in decreasing order according to the absolute values. Error bars on experimental data represent ten standard deviations. Each layout pattern under x-axis denote a Pauli string with each qubit colored according to the corresponding Pauli operator.

B. Deviation of J_y for the diverging flow

We generate a circuit for encoding the 2D diverging flow by applying an extra error gate after each single-qubit gate on all qubits, which yields a similar x-averaged profile of J_y with the experimental result in Fig. S9.

C. Energy spectrum for the decaying vortex

We calculate the energy spectrum

$$E_k(k) \equiv \frac{1}{2}\sum_{\boldsymbol{k}'} |\hat{\boldsymbol{u}}(\boldsymbol{k}')|^2 \delta(|\boldsymbol{k}'| - k) \tag{S42}$$

for the 2D decaying vortex, where $\hat{\boldsymbol{u}}$ denotes the Fourier coefficients of the velocity field $\boldsymbol{u}$. We observe that the energy spectrum E_k of the noisy experimental data, which contains turbulent artifacts due to quantum gate noise, exhibits the $k^{-5/3}$ scaling law as in classical homogeneous isotropic turbulence [S16]. The $-5/3$ scaling law for experimental data at $t = 0$ and $t = \pi/4$ is similar to that at $t = \pi/2$ (not shown).

5. SUPPLEMENTARY NOTE 5: COMPLEXITY ANALYSIS

We analyze the algorithm complexities of simulating fluid flows via Hamiltonian simulation. Consider a D-dimensional flow using nD qubits with $N = 2^n$ grid points in each dimension and total number $N^D = 2^{nD}$ of grid points.

First, we address the time complexity of state preparation. The preparation of an initial state involves breaking down each unitary transformation on nD qubits. Various quantum algorithms and their complexities for state preparation are summarized in Ref. [S17]. Currently, no quantum algorithm achieves simultaneous logarithmic time complexity in terms of N^D, κ, and $1/\varepsilon$, where κ denotes the condition number of the state vector, and ε characterizes accuracy. In general, preparing any nD-qubit initial state needs a prohibitive circuit depth of $O(2^{nD})$, which challenges the quantum advantage. This problem can be addressed through the implementation of quantum random access memory [S18]. Additionally, variational quantum algorithms can facilitate generating the approximate quantum circuit for a given initial velocity with a polynomial scale.

Second, we analyze the time complexity of state evolution. The quantum gate complexity per temporal increment is $S_q = O(n^2 D)$ [S19]. By contrast, the corresponding complexity using the fast Fourier transform is $S_c = O(nD2^{nD})$ in classical computing. For the state evolution, quantum computing demonstrates a remarkable speedup, with the ratio $R_q = O(2^{nD}/n)$ compared to its classical counterpart.

Third, we analyze the measurement complexity. To reconstruct the entire flow field, the expectation of $O(4^{nD})$ Pauli strings must be measured. Each measurement involves $O(100 \times 2^{nD})$ single shots to build the probability distribution and is repeated

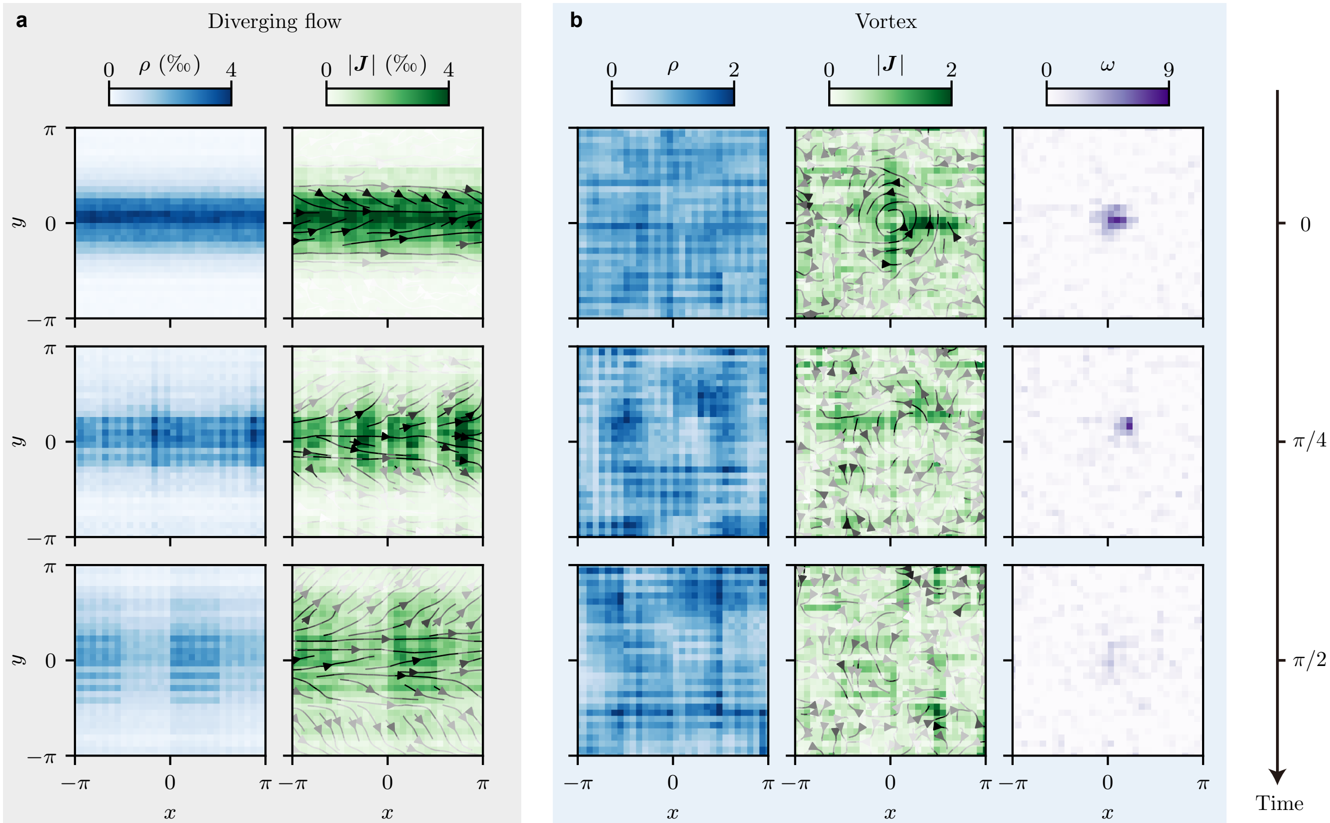

Figure S7. Experimental results on the temporal evolution (from top to bottom) of flow fields. (a) Density (left) and momentum (right) contours with streamlines for the 2D diverging flow. (b) Density (left), momentum (middle), and vorticity (right) contours for the 2D vortex.

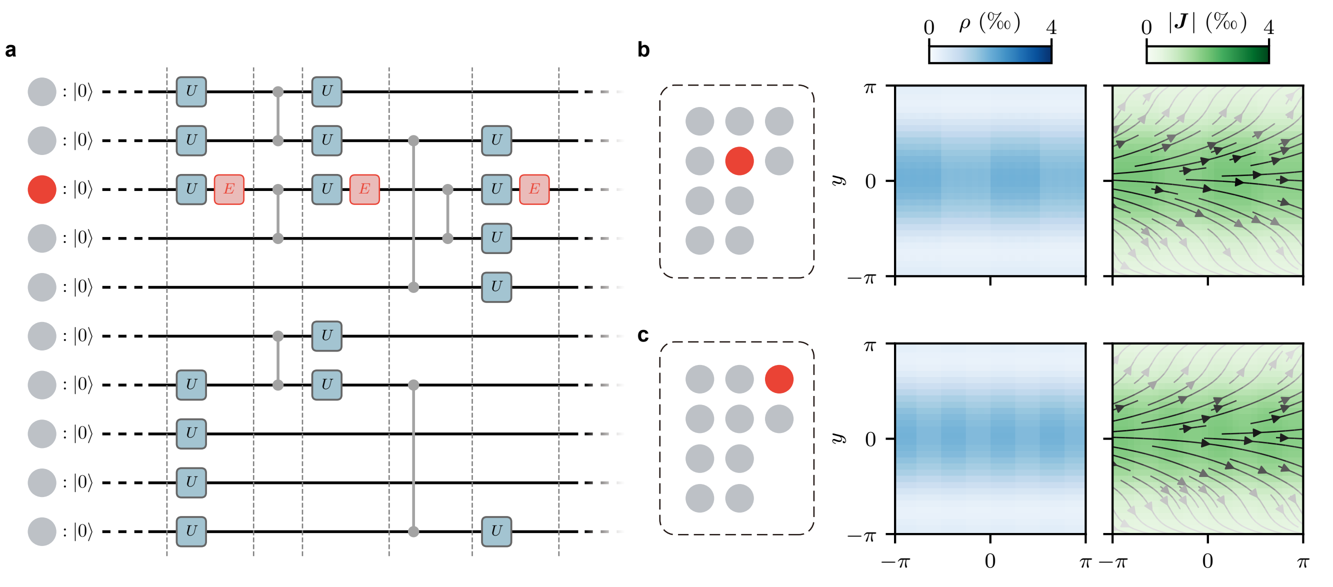

Figure S8. Numerical simulations for showing the origin of stripe-like artifacts in the experimental results for the 2D diverging flow. (a) We apply an extra error gate after each single-qubit gate on a certain qubit as a local perturbation. The error gate is selected as $R_x(0.025)$ with an equivalent error rate of around 2×10^{-4}. (b,c) Simulation results for the evolution of the 2D diverging flow at $t = \pi/2$ with two different choices of the error qubit as shown in dashed rectangles.

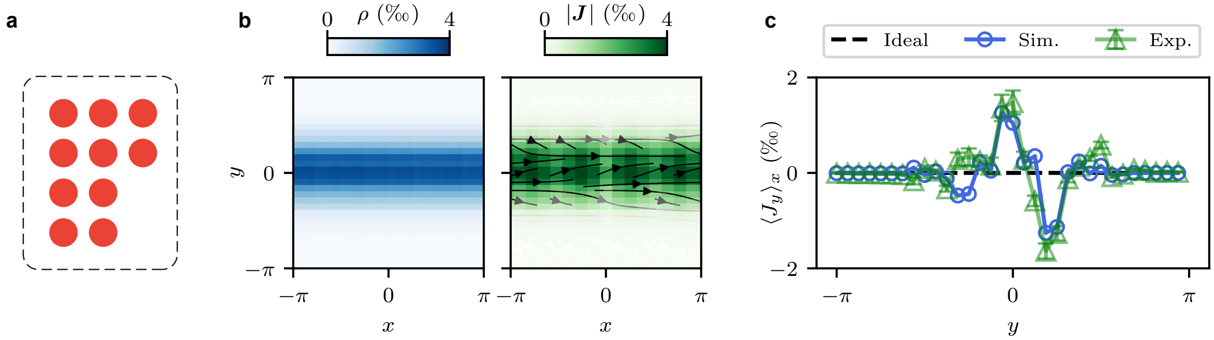

Figure S9. Numerical simulations for showing the origin of the notable deviation of J_y in the experimental results for the 2D diverging flow. (a) Similar to Fig. S8, all qubits in red indicate that each single-qubit gate in the circuit is appended with an error gate. Error gates are selected as $U(\theta, \phi, \lambda)$ with parameters randomly sampled from uniform distribution of $[-0.045, 0.045]$. The average equivalent error rates are around 5×10^{-4}. To obtain the desired x-averaged profile of J_y, we have carefully searched the random seed. (b) Reconstructed density (left) and momentum (right) contours from the numerical simulation. (c) Comparison of the x-averaged profile of J_y among results from the exact solution (black), simulation (blue), and experiment (green).

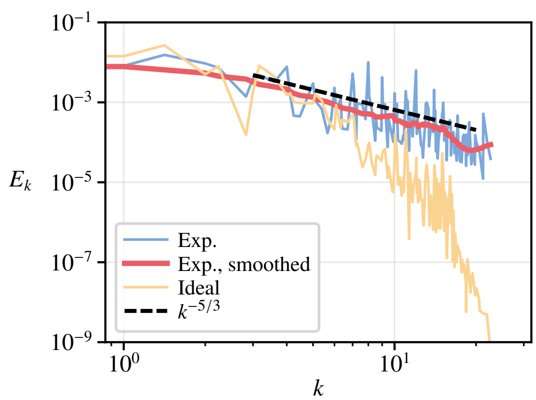

Figure S10. Energy spectra for the 2D decaying vortex at $t = \pi/2$, including the experimental data, the smoothed data via the Savitzky-Golay filter, and the ideal result. The experimental data, with the turbulent artifacts induced by quantum gate noises, adheres to the $k^{-5/3}$ scaling law.

for several times. This requirement results in high time complexity for the measurement. Therefore, it is imperative to devise measurement operators that either restrict flow statistics to a minimal set of qubits or allow an expansion into polynomial-scale Pauli strings.

SUPPLEMENTARY REFERENCES

[S1] E. Madelung, Quantentheorie in hydrodynamischer form, Z. Phys. **40**, 322 (1927).
[S2] E. J. Mueller and T.-L. Ho, Two-component Bose-Einstein condensates with a large number of vortices, Phys. Rev. Lett. **88**, 180403 (2002).
[S3] K. Kasamatsu, M. Tsubota, and M. Ueda, Vortex phase diagram in rotating two-component Bose-Einstein condensates, Phys. Rev. Lett. **91**, 150406 (2003).
[S4] Z. Meng and Y. Yang, Quantum computing of fluid dynamics using the hydrodynamic Schrödinger equation, Phys. Rev. Res. **5**, 033182 (2023).
[S5] H. Kedia, D. Foster, M. R. Dennis, and W. T. M. Irvine, Weaving knotted vector fields with tunable helicity, Phys. Rev. Lett. **117**, 274501 (2016).
[S6] Z. Lu and Y. Yang, Quantum computing of reacting flows via Hamiltonian simulation (2023), arXiv:2312.07893.
[S7] R. Jozsa, Quantum algorithms and the Fourier transform, Proc. R. Soc. Lond. A. **454**, 323 (1998).
[S8] Y. S. Weinstein, M. A. Pravia, E. M. Fortunato, S. Lloyd, and D. G. Cory, Implementation of the quantum Fourier transform, Phys. Rev. Lett. **86**, 1889 (2001).
[S9] N. A. Nemkov, E. O. Kiktenko, I. A. Luchnikov, and A. K. Fedorov, Efficient variational synthesis of quantum circuits with coherent multi-start optimization, Quantum **7**, 993 (2023).

[S10] S. Xu, Z.-Z. Sun, K. Wang, *et al.*, Digital Simulation of Projective Non-Abelian Anyons with 68 Superconducting Qubits, Chin. Phys. Lett. **40**, 060301 (2023).
[S11] D. C. McKay, C. J. Wood, S. Sheldon, J. M. Chow, and J. M. Gambetta, Efficient Z gates for quantum computing, Phys. Rev. A **96**, 022330 (2017).
[S12] C. Song, K. Xu, W. Liu, C.-P. Yang, S.-B. Zheng, H. Deng, Q. Xie, K. Huang, Q. Guo, L. Zhang, *et al.*, 10-Qubit Entanglement and Parallel Logic Operations with a Superconducting Circuit, Phys. Rev. Lett. **119**, 180511 (2017).
[S13] W. Ren, W. Li, S. Xu, *et al.*, Experimental Quantum Adversarial Learning with Programmable Superconducting Qubits, Nat. Comput. Sci. **2**, 711 (2022).
[S14] S. Boixo, S. V. Isakov, V. N. Smelyanskiy, R. Babbush, N. Ding, Z. Jiang, M. J. Bremner, J. M. Martinis, and H. Neven, Characterizing quantum supremacy in near-term devices, Nat. Phys. **14**, 595 (2018).
[S15] F. Arute, K. Arya, R. Babbush, D. Bacon, J. C. Bardin, R. Barends, R. Biswas, S. Boixo, F. G. S. L. Brandao, D. A. Buell, *et al.*, Quantum supremacy using a programmable superconducting processor, Nature **574**, 505 (2019).
[S16] S. B. Pope, *Turbulent Flows* (Cambridge University Press, 2000).
[S17] C. Shao, Quantum algorithms to matrix multiplication (2018), arXiv:1803.01601.
[S18] V. Giovannetti, S. Lloyd, and L. Maccone, Quantum random access memory, Phys. Rev. Lett. **100**, 160501 (2008).
[S19] M. A. Nielsen and I. L. Chuang, *Quantum Computation and Quantum Information*, 10th ed. (Cambridge University Press, New York, 2010).